Tunable broadband light emission from graphene

Lavinia Ghirardini[1,§], Eva A. A. Pogna[1,2,§], Giancarlo Soavi[3,4,§], Andrea Tomadin[5], Paolo Biagioni[1], Stefano Dal Conte[1], Sandro Mignuzzi[3], Domenico De Fazio[3,6], Takashi Taniguchi,[7] Kenji Watanabe,[8] Lamberto Duò[1], Marco Finazzi[1], Marco Polini[5], Andrea C. Ferrari[3], Giulio Cerullo[1*], Michele Celebrano[1*]

[1]Politecnico di Milano, Physics Department, Piazza Leonardo Da Vinci 32, 20133 Milano (Italy)

[2]CNR-NANO, NEST, Piazza San Silvestro 12, I-56127 Pisa

[3]Cambridge Graphene Centre, University of Cambridge, 9 JJ Thomson Avenue, Cambridge CB3 0FA, UK

[4]Institute for Solid State Physics, Abbe Center of Photonics, Friedrich-Schiller-University Jena, Max-Wien-Platz 1, 07743, Jena, Germany

[5]Physics Department, Pisa University, Largo Bruno Pontecorvo 3, 56127 Pisa, Italy

[6]ICFO, Mediterranean Technology Park, Av. Carl Friedrich Gauss, 3 08860 Castelldefels (Barcelona), Spain.

[7]International Center for Materials Nanoarchitectonics, National Institute for Materials Science, 1-1 Namiki, Tsukuba 305-0044, Japan

[8]Research Center for Functional Materials, National Institute for Materials Science, 1-1 Namiki, Tsukuba 305-0044, Japan

[§]These authors equally contributed to this work.

[*]email: michele.celebrano@polimi.it; giulio.cerullo@polimi.it

Abstract

Graphene is an ideal material for integrated nonlinear optics thanks to its strong light-matter interaction and large nonlinear optical susceptibility. Graphene has been used in optical modulators, saturable absorbers, nonlinear frequency converters, and broadband light emitters. For the latter application, a key requirement is the ability to control and engineer the emission wavelength and bandwidth, as well as the electronic temperature of graphene. Here, we demonstrate that the emission wavelength of graphene's broadband hot carrier photoluminescence can be tuned by integration on photonic cavities, while thermal management can be achieved by out-of-plane heat transfer to hexagonal boron nitride. Our results pave the way to graphene-based ultrafast broadband light emitters with tunable emission.

1. Introduction

The opto-electronic properties of graphene [1] are ideal for a variety of applications [2], such as optical modulators [3-5], saturable absorbers [6], plasmonic devices [7,8], and various types of broadband detectors [9], working from the THz [10] to the visible(VIS)/infrared(IR) spectral range [11-13]. Despite being atomically thin, single-layer graphene (SLG) absorbs 2.3% per layer in the VIS (400-750 nm)[14] and near-IR (NIR, 1000-2400 nm) [15], and has a large nonlinear optical response (e.g. third order nonlinear susceptibility $\chi^{(3)} \sim 10^{-19}$ - 10^{-16} m^2V^{-2} in the VIS and NIR depending on excitation photon energy and doping [16, 17]), paving the way to new applications such as gate-tunable frequency converters [16 - 18] and broadband light-emitters [19 - 27].

In intrinsic SLG, due to the absence of a gap and the linear dispersion of conduction and valence bands around the Dirac points, the massless Dirac Fermions have a spectrally flat optical response [14,15,28]. In principle, the gapless nature of SLG along with the ultrafast charge carrier recombination are expected to inhibit radiative recombination processes [19], while black-body radiation can still occur due to intra-band radiative transitions, Fig. 1a. Nevertheless, broadband light emission from excited charge carriers, i.e. hot carrier photoluminescence (HotPL), can be achieved in SLG via radiative recombination of hot electrons (HEs) [19,20,29] characterized by a non-equilibrium thermal distribution [16,17,30]. A key feature of SLG-based thermal emitters is the broad emission at room-temperature (RT), which can be extended from THz [31] to the visible range [24], by controlling the HEs temperature T_e. An out-of-equilibrium distribution of electrons can be induced both by electrical [24-27] and ultrafast (~100fs) optical [19-21] excitation. Electrically driven HotPL emission can be controlled by current pulse duration [32] and SLG channel dimension [27]. SLG can sustain high current densities (up to ~10^8 A/cm^2) [26] and reaches high (~10^8 A/cm^2) saturation current density [21,24]. However, in SLG on SiO_2/Si the heat dissipation to the substrate limits the achievable T_e (up to 600K [21] corresponding to an emission spectrum spanning the mid-IR and NIR). Using suspended architectures, it is possible to reach higher T_e (up to 2880K [24]), thus emission in the VIS range. Manipulation of the thermal emission spectrum in SLG was obtained exploiting interference in trench structures [24], integration into a dielectric optical cavity [26], using frequency-selective metasurfaces [33] and sub-wavelength photonic crystals [27]. Photoexcitation with femtosecond pulses produces high $T_e > 1000$ K [16, 19], corresponding to emission extended to the VIS range (up to 3.5 eV) [16,17,19,34].

Following ultrafast-light absorption by vertical transitions within the Dirac cones, electrons are brought in a non-equilibrium thermal distribution (see Fig. 1b), which thermalizes via electron-electron scattering in a very short time (<20 fs) [35] into a hot Fermi Dirac (FD) distribution (i.e. a non-equilibrium thermal distribution) with T_e that can reach 2000-3000 K [16, 17, 19, 34], Fig.1c). The HEs then thermalize with the lattice on a ps timescale [354,35], via emission of optical and acoustic phonons [35]. Due to the short lifetime of HEs in SLG [354, 365], thermal emission via HotPL has the advantage of enabling ultra-fast modulation comparable to the inverse of the HEs recombination (~1ps) [26,38], thus modulation frequencies up to THz, could be achieved, and modulation frequencies up to tens of GHz were reported in SLG [26]. This makes SLG-based light emitters promising for on-chip light sources in high -speed (GHz-THz) communication and as alternative to lasers and LEDs in Si photonics [3,5]. SLG-based devices hold promise also in gas sensing applications[39,40], where state of the art devices exploit thermal emitters based on micro-electro-mechanical systems (MEMS)[39], which feature modulation frequencies ~100 Hz [39]. In this framework, absorption enhancement, e.g. by integration of SLG in optical cavities [41] or photonic crystals [42], constitutes a promising route to increase emissivity. This strategy, previously demonstrated with thermal emitters based on nanostructures [43], MEMS [40] and quantum wells [44], can mitigate the low (~4.5×10^{-3}) efficiency (i.e. ratio between optically radiated and applied electrical power) of thermal emitters based on SLG [24]. In the IR spectral region, gate-tunable absorption>90% was reported in SLG-based thermal emitters embedded in photonic cavities[45,46], suggesting that an emissivity close to one could be achieved [45, 46].

Here we investigate the nonlinear light emission of SLG, following NIR excitation with 150 fs pulses at 1554 nm (0.8 eV). We show emission wavelength and bandwidth tuning of the HotPL, modulated by both photonic cavity effects and T_e engineering, Fig. 1d-f. To this aim, we compare samples produced by micromechanical cleavage (MC) of bulk crystals [47], both pristine (MC-SLG) and encapsulated (hBN/SLG/hBN) in two ~ 10-nm-thick layers of hBN transferred on a 285-nm-thick SiO_2 layer on Si, with SLG grown by chemical vapor deposition (CVD-SLG), transferred either on SiO_2/Si or on glass. This allows us to simultaneously investigate the effects of substrate, defects and T_e on the SLG HotPL. The HotPL spectral emission profile is reshaped by photonic cavity effects induced by the substrate (see Fig. 1e), as confirmed by a model describing the SLG HotPL combining Finite Difference Time Domain (FDTD) simulations, accounting for the photonic response of the substrate, with a semiclassical expression for the emission spectrum. We also demonstrate, through both HotPL and third harmonic generation (THG) measurements, that hBN allows to further tune the HotPL emission, thanks to the cooling process occurring between the hyperbolic phonons in hBN and

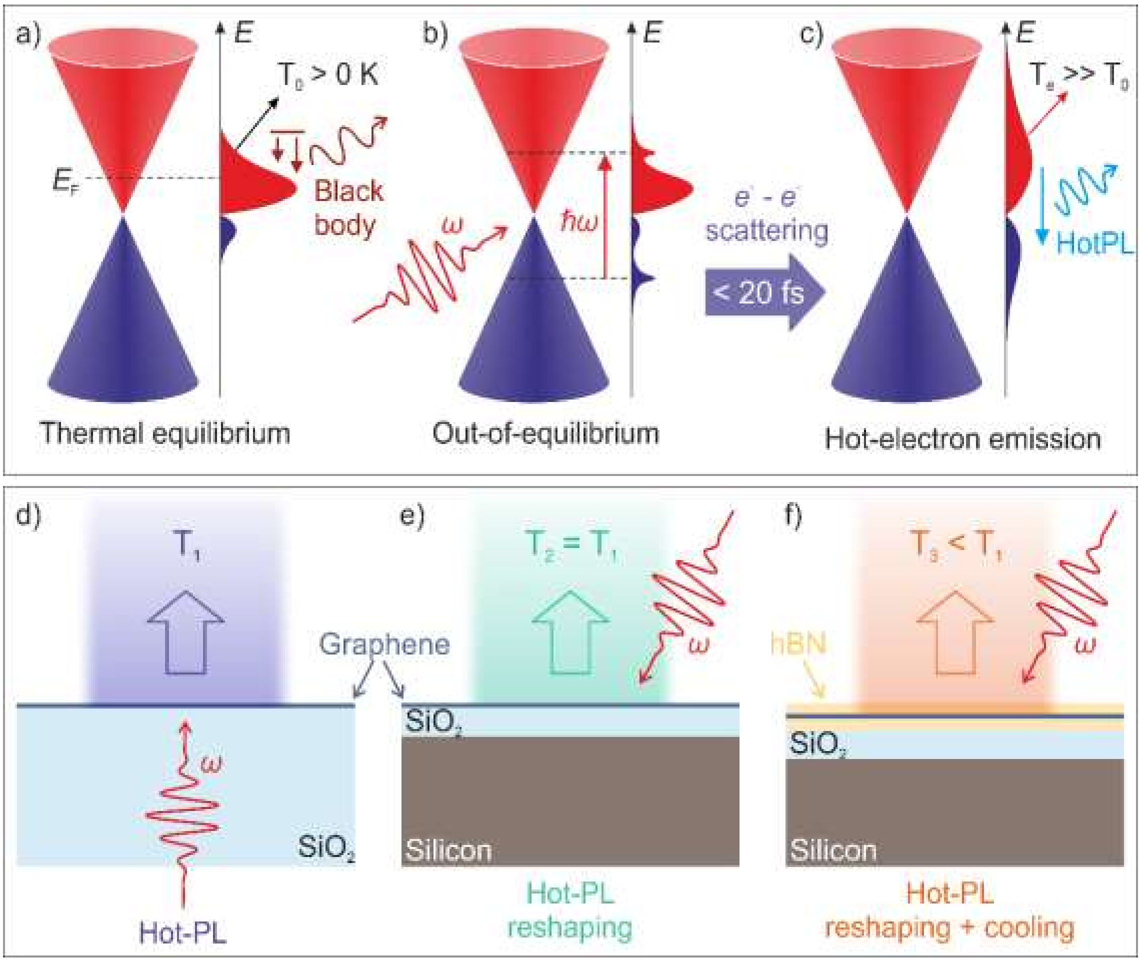

Figure 1. HotPL emission mechanism and tuning principles. a-c) Sketches of n-doped SLG conical bands in the vicinity of the Dirac points and of e (red)/h(blue) density distribution (i.e. the e/h distribution multiplied by the density of states), at various stages of the photoexcited HotPL dynamics. a) The electron density distribution intrinsic broadening for $T_0 > 0$ K causes black-body emission in SLG. b) Upon ultrafast laser excitation, out-of-equilibrium charge distributions are formed on sub-20-fs time scales. c) At time scales comparable with our pulse duration the e distribution thermalizes, resulting in $T_e >> T_0$ and in two different chemical potentials for e/h. The increased h density in the valence band compared to the equilibrium situation (a) allows for the HE radiative recombination, leading to photoluminescence emission (HotPL). d) HotPL emission upon ultrafast laser excitation in SLG on SiO_2 at $T_e = T_1 >> T_0$. e) The same process in SLG on SiO_2/Si at the same $T_e = T_2 = T_1$ is spectrally reshaped by cavity effects. f) HotPL is further tuned when SLG is encapsulated in a double layer of hBN, thanks to the cooling effects between HE and hyperbolic phonons in hBN, which lead to $T_e = T_3 < T_1$.

the SLG HE, Fig. 1f. Our approach can describe the incoherent emission from any layered material (LM) coupled to any substrate and optical environment, and is thus relevant for the design of photonic devices based on LMs.

2. Results and discussion

2.1. Fabrication and characterization of the SLG devices

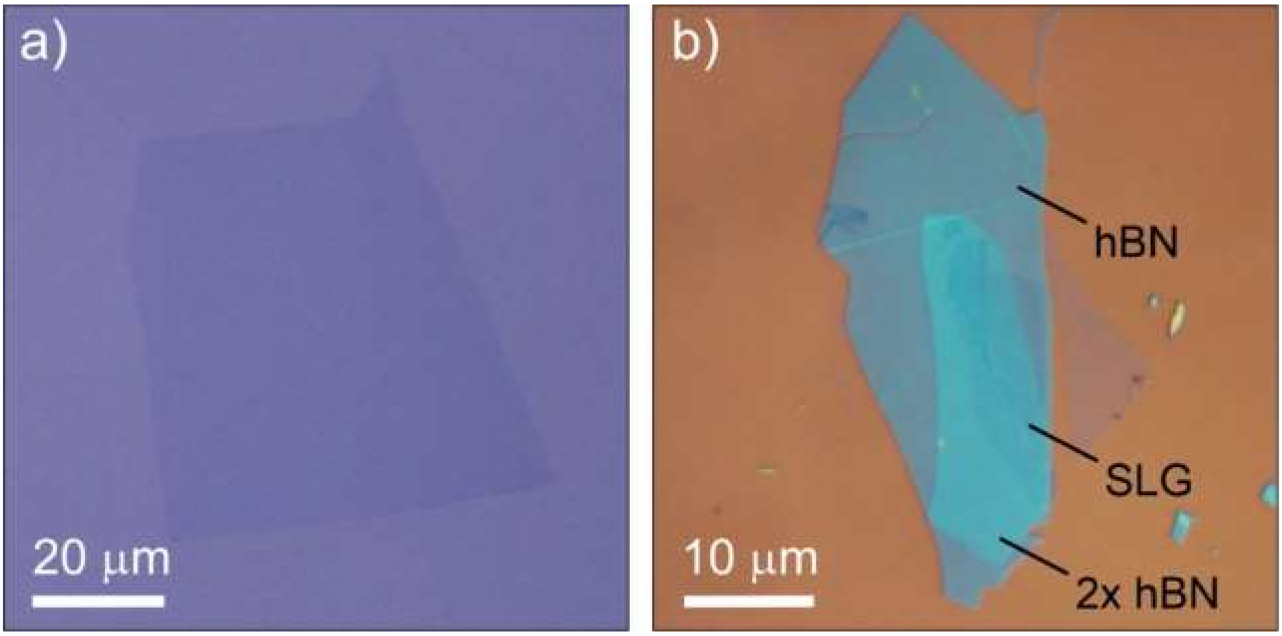

Figure 2. Microscope images of representative samples. a) MC-SLG. b) hBN/SLG/hBN. SLG on the right side of the image is embedded between wider (on top) and smaller (on the bottom) 10nm thick hBN flakes.

CVD-SLG is grown on Cu as described in Ref. [48]. A Cu foil (99.8% pure) is placed in a furnace and annealed at 1000 °C in a 20 standard cubic centimetres per minute (sccm) hydrogen flux at ~ 196 mTorr for 30mins. The growth is initiated by adding a 5 sccm CH_4 for 30 min. SLG is then transferred on 200-µm-thick SiO_2 coverslips or 285-nm-thick SiO_2 on Si by polymer-assisted Cu wet etching [48], using polymethyl methacrylate (PMMA). Direct growth on SiO_2/Si would have not allowed to obtain SLG with low defects density [49,50]. Flakes of hBN and SLG are also prepared by MC [46] of bulk graphite (NGS Naturgraphit) and hBN using adhesive tape. hBN crystals are grown under high pressure and high temperature conditions, as for Ref.51. SLG and hBN flakes are identified prior to transfer by a combination of optical microscopy [52] and Raman spectroscopy [53-56]. We use ~ 10-nm-thick hBN flakes as they provide sufficient screening from charge impurities in the underlying substrate [57,58]. Fig. 2 shows representative microscope images of MC-SLG and hBN/SLG/hBN samples. The Raman spectra of all samples, measured with a Renishaw Raman inVia

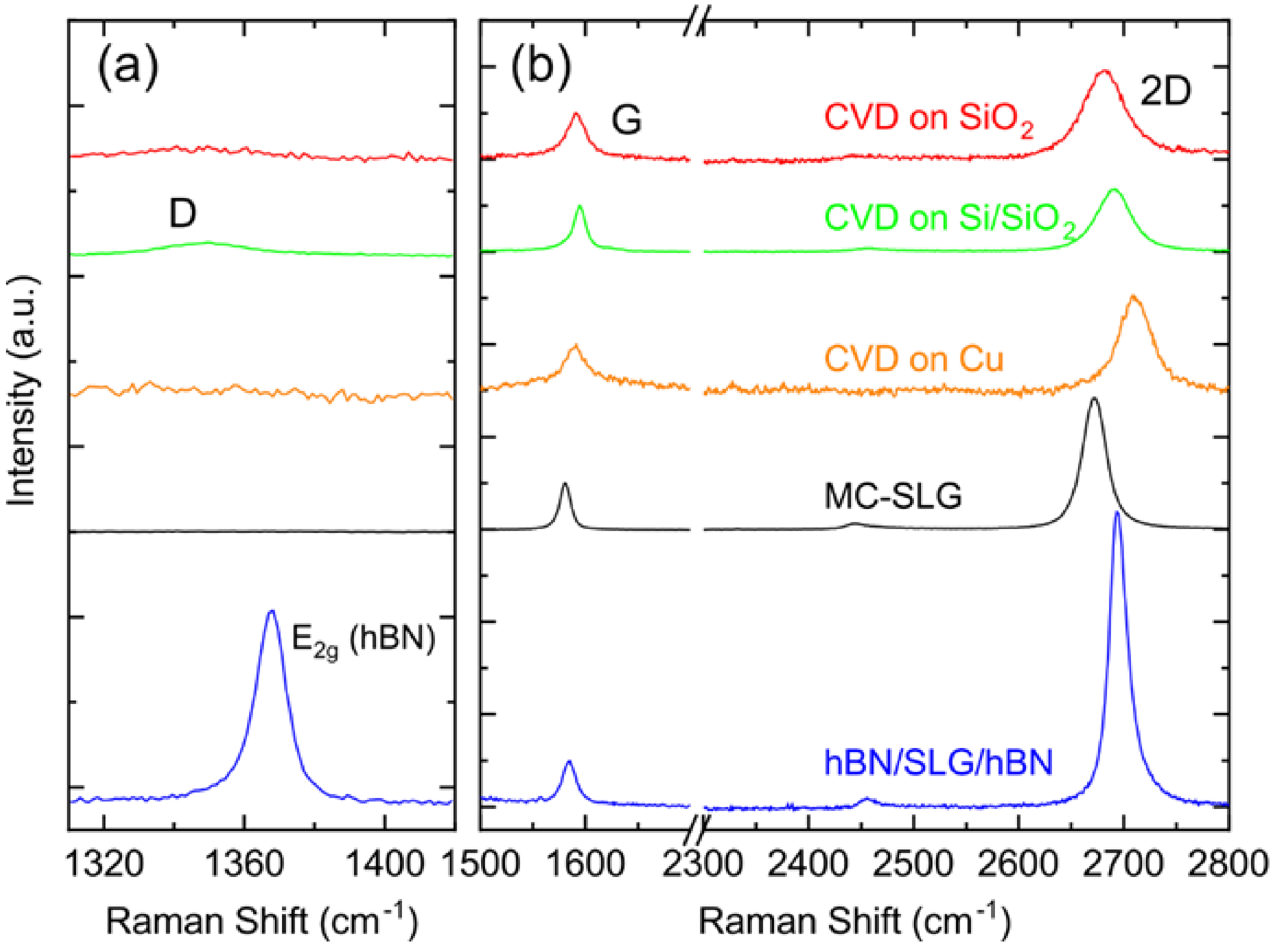

Figure 3. Raman spectroscopy. Raman spectra of SLG samples at 514 nm excitation. All spectra in (a) and (b) are normalized to the G peak intensity.

spectrometer equipped with a 50x objective at 514 nm, are reported in Fig. 3. The orange curve shows the Raman spectrum of SLG on Cu before transfer, after subtraction of the PL from Cu [59]. The spectrum shows a single sharp Lorentzian 2D peak with full width at half maximum FWHM(2D)~33 cm^{-1} and peak position Pos(2D)~ 2710 cm^{-1}, which is a fingerprint of SLG [53]. The D peak is negligible. In hBN/SLG/hBN, the hBN E$_{2g}$ Raman peak is a combination of those from both top and bottom hBN. This yields a single peak with position Pos(E$_{2g}$)~1367cm^{-1} and FWHM(E$_{2g}$)~9.8cm^{-1}, as expected for bulk hBN [53, 55].

Table 1 summarizes the Raman fit parameters and the resulting Fermi energy, E$_F$, carrier concentration, *n*, doping type (*n* or *p*), strain, and defect density, n_D. E$_F$ is estimated from A(2D)/A(G), I(2D)/I(G) (A peak area and I peak intensity) and FWHM(G) [60,61], while the strain is estimated from Pos(G) as discussed in Refs. [62,63]. The biaxial strain can be differentiated from the uniaxial

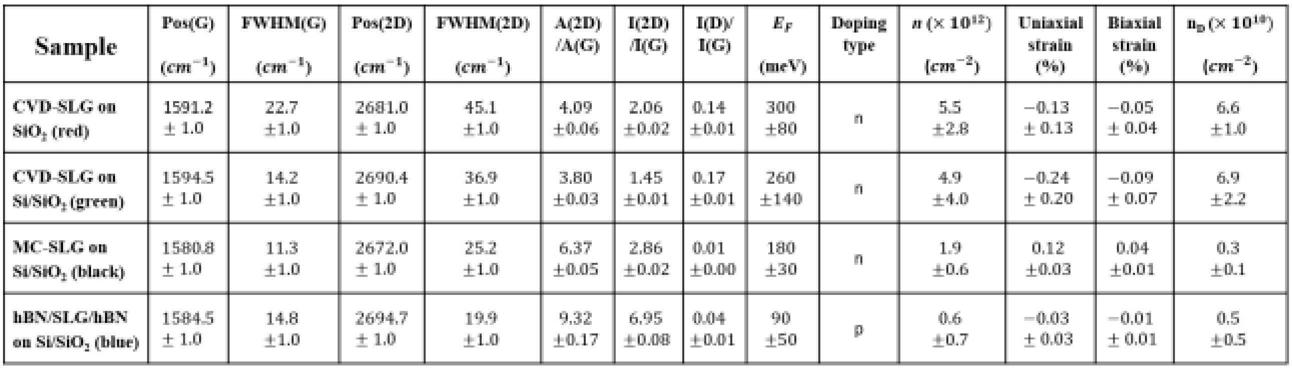

Sample	Pos(G) (cm^{-1})	FWHM(G) (cm^{-1})	Pos(2D) (cm^{-1})	FWHM(2D) (cm^{-1})	A(2D) /A(G)	I(2D) /I(G)	I(D)/ I(G)	E_F (meV)	Doping type	n (× 10^{12}) (cm^{-2})	Uniaxial strain (%)	Biaxial strain (%)	n_D (× 10^{10}) (cm^{-2})
CVD-SLG on SiO_2 (red)	1591.2 ± 1.0	22.7 ±1.0	2681.0 ± 1.0	45.1 ±1.0	4.09 ±0.06	2.06 ±0.02	0.14 ±0.01	300 ±80	n	5.5 ±2.8	−0.13 ± 0.13	−0.05 ± 0.04	6.6 ±1.0
CVD-SLG on Si/SiO_2 (green)	1594.5 ± 1.0	14.2 ±1.0	2690.4 ± 1.0	36.9 ±1.0	3.80 ±0.03	1.45 ±0.01	0.17 ±0.01	260 ±140	n	4.9 ±4.0	−0.24 ± 0.20	−0.09 ± 0.07	6.9 ±2.2
MC-SLG on Si/SiO_2 (black)	1580.8 ± 1.0	11.3 ±1.0	2672.0 ± 1.0	25.2 ±1.0	6.37 ±0.05	2.86 ±0.02	0.01 ±0.00	180 ±30	n	1.9 ±0.6	0.12 ±0.03	0.04 ±0.01	0.3 ±0.1
hBN/SLG/hBN on Si/SiO_2 (blue)	1584.5 ± 1.0	14.8 ±1.0	2694.7 ± 1.0	19.9 ±1.0	9.32 ±0.17	6.95 ±0.08	0.04 ±0.01	90 ±50	p	0.6 ±0.7	−0.03 ± 0.03	−0.01 ± 0.01	0.5 ±0.5

Table 1. Raman analysis. Raman peaks fit parameters and corresponding E_F, doping concentration n, and defects density n_D, with associated error (±).

one by the absence of G-peak splitting with increasing strain, however at low (≲0.5%) strain the splitting cannot be resolved. For uniaxial(biaxial) strain, Pos(G) shifts by ~23(60)cm^{-1}/% [62,63]. Since Pos(G) depends on both E_F and strain [60,62], to retrieve the contribution of strain only, we first derive E_F from A(2D)/A(G), I(2D)/I(G) and FWHM(G), which are independent on strain [60,61,64], and then calculate Pos(G) corresponding this E_F. The strain is then retrieved from the difference between the experimental and calculated Pos(G). The strain values in Table 1 are positive (negative) for tensile (compressive) strain. The doping type is estimated from Pos(2D), which decreases from p to n doping [60]. Note that Pos(2D) shifts by ~83(191) cm-1/% with uniaxial (biaxial) strain [62]. We thus calculate the contribution of strain to Pos(2D) and subtract this value from the experimental Pos(2D) to obtain the doping type. Finally, the defect density n_D, is estimated from I(D)/I(G) and E_F [64,66]. The error bars in Table 1 are calculated from the standard error of the fits, the spectrometer resolution (~1 cm^{-1}) and the uncertainty associated with the methods to estimate E_F from Pos(G), FWHM(G), I(2D)/I(G), A(2D)/A(G) and Pos(2D).

To verify the optical uniformity and spatial homogeneity of the samples, THG maps are acquired using a nonlinear optical microscope equipped with a 0.85 numerical aperture (NA) air objective for both IR illumination, with 150 fs pulses at 1554 nm from an Er- doped fiber laser, and light collection. The power impinging on the samples ranges from 300 to 700 μW (pump fluence ~ 2.1–4.9 J/m^2). The sample is mounted upside-down on a piezo stage to acquire nonlinear emission spatial maps. The nonlinear emission is collected by the objective in reflection, and deflected to the detection path by a dichroic mirror (cut-off wavelength ~1000nm), to reject the residual laser radiation. A flip mirror allows selecting between a VIS-NIR spectrometer, to record the whole emission spectrum, and a Si-based Single Photon Avalanche Detector (SPAD) for THG detection. For THG measurements a narrow-band filter (NBF, with central wavelength 520nm (2.4 eV), and bandwidth 40 nm (0.18 eV)) is in front of the SPAD. All samples are excited from the air side. THG maps are acquired by imaging 80 × 80 μm^2 areas on the SLG edge to enable simultaneous recording of the SiO_2 signal as a background to be subtracted from the total signal collected on SLG.

Figs. 4a-c show 10×10 μm^2 areas of the overall THG maps for MC-SLG on SiO_2/Si (Fig. 4a), CVD-SLG on SiO_2/Si (Fig. 4b), and hBN/SLG/hBN on SiO_2/Si (Fig. 4c). The THG and PL emission from the bare SiO_2/Si (darker areas in the maps) are about one order of magnitude lower than the SLG signal in the spectral window set by the filter. The THG conversion efficiency (THGE), defined as $\eta^{THG} = I_{3\omega}/I_{\omega}$ [16], where I_{ω} and $I_{3\omega}$ are the incident and THG power, respectively, is calculated by computing the total number of photons emitted at the peak fluence~ 4.9 J/m^2 (700 μW), about a factor two below the damage threshold of SLG (~ 10 J/m^2) for 150-fs pump pulses with a repetition rate~ 80MHz. This is the fluence at which the THG signal degrades after a 1min irradiation.

The total absolute THG emitted power is estimated by taking into account the overall transmission efficiency of our apparatus and evaluating the collected fraction of the THG power. We model the emission from SLG as that of a dipole parallel to the substrate using FDTD simulations [67]. We estimate an overall photon collection efficiency within the objective NA of ~20% for SLG on SiO_2/Si, and ~10% for hBN/SLG/hBN on SiO_2/Si. The drop in collection efficiency at the THG wavelength for hBN/SLG/hBN on SiO_2/Si is due to presence of the 2 hBN layers, which redirect half of the THG out of the collection NA (see Fig.5). This, together with the objective transmission at the THG wavelength (~80%), the optical throughput in the detection path (~ 20%), the single-photon avalanche detector quantum yield (~ 50%) and its filling factor (~ 50%), determines a drop by over two orders of magnitude in the number of detected photons with respect to the emitted ones. Thus,

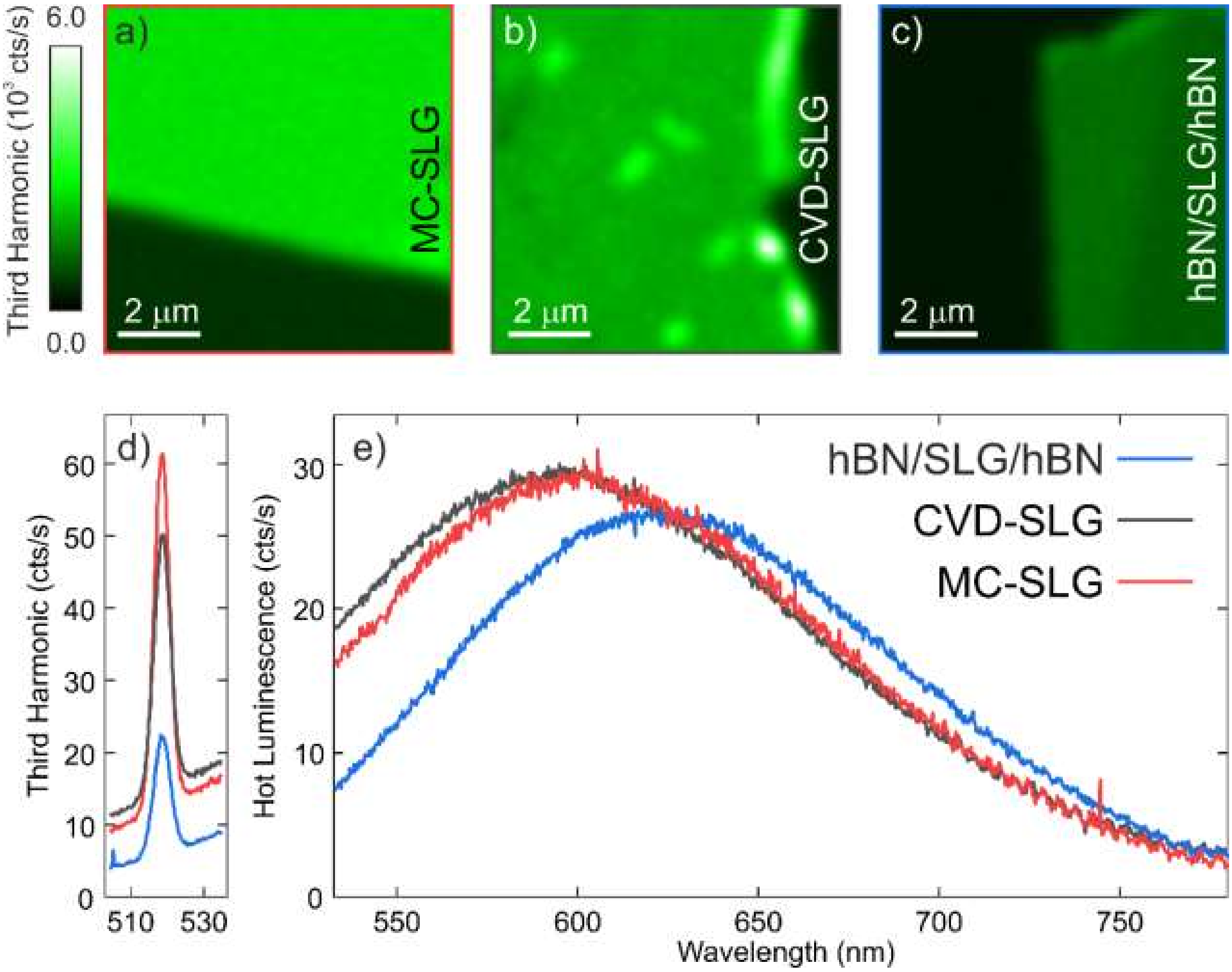

Figure 4. THG maps for (a) MC-SLG, (b) CVD-SLG, (c) and hBN/SLG/hBN on SiO_2/Si. The scanned region is 10 × 10 μm^2. d) THG peaking at ~ 518 nm for MC-SLG (red), CVD-SLG (grey) and hBN/SLG/hBN (blue). e) The visible-NIR portion of the spectrum, between 500 and 800nm, showing HotPL spectra.

the total THG emitted power $I_{3\omega}$ is~160, 130, 45 fW for MC-SLG, CVD- SLG and hBN/SLG/hBN, respectively, for an average pump power $I_\omega \sim 700$ μW. This defines higher-bound values for $\eta^{THG} \sim 2.3 \times 10^{-10}$, 1.8×10^{-10} and 1.3×10^{-10} for the three samples, respectively, in agreement with our previous measurements [16, 17]. η^{THG} decreases going from MC-SLG to CVD-SLG, to hBN/SLG/hBN. In general, η^{THG} depends on T_e, E_F, I_ω, and on the incident photon energy $\hbar\omega$ [16]. Since I_ω and $\hbar\omega$ are, we attribute the different η^{THG} to variations of T_e and E_F.

2.2. Reshaping of the HotPL emission with a photonic cavity

To further investigate the effect of the photonic environment on the nonlinear emission properties of SLG, we also record the nonlinear emission spectra from each sample with an integration time of 10s, while raster-scanning over 10 × 10 μm^2. This is done to minimize photodamage and suppress the influence of intensity hot-spots resulting from nonlinear field enhancements associated with defects [68]. The nonlinear emission from the substrate, evaluated in a similar way, features mostly ambient light coming from non-perfect shielding of the spectrometer, along with an extremely weak (~2 orders of magnitude lower than the HotPL signal) multi-photon PL coming from SiO_2 [69]. While they cannot be employed for calibration, the background spectra are subtracted to obtain clean HotPL and THG spectra.

The emission spectra are shown in Figs. 4d,e and identify a THG peak~ 518 nm (~ 2.4 eV) which corresponds to one third of the 1554nm wavelength of the pump beam, as expected for this nonlinear process [70]. The HotPL signal arising from photoexcited HEs in SLG gives a broad feature in the 500-800 nm spectral range. Refs.19, 20, 34 reported ultrafast HotPL in MC SLG both on mica and Si/SiO_2 for 800 nm (1.55 eV) excitation, showing an exponential decay at increasing photon energies. A similar behavior was reported in electroluminescence experiments [24], and modeled within a semi-classical approach to account for the out-of-equilibrium condition of the system [24]. The HotPL spectra in Fig.3e show instead a maximum between 600 nm (2.06 eV) and 700 nm (1.77 eV), depending on sample and pump fluence. We attribute this behavior, which qualitatively differs from those reported in Refs. 19, 20, 25, 34, to the different excitation photon energy and sample geometry. The SiO_2 thickness (285nm) is comparable with the VIS and NIR wavelengths (400-1000 nm). Such thin-film interference effects are often exploited in photonic devices to optimize the in- and out-coupling of light [71].

To investigate the spectral reshaping of the HotPL emission from SLG, we compare the emission from two CVD SLG samples deposited on different substrates: SiO_2/Si or a 200 μm SiO_2 coverslip (see Figs. 5a,b). In the second case, the spectrum is acquired by adapting the setup in Fig.

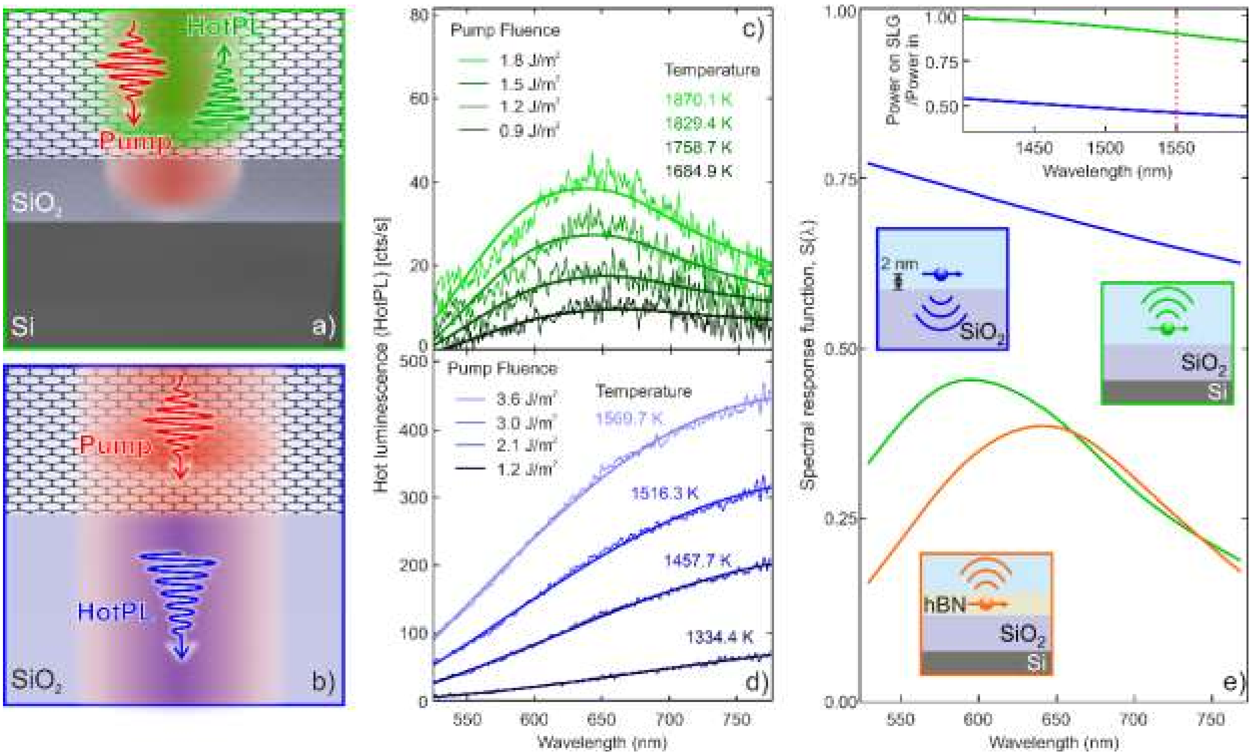

Figure 5. Sketches of CVD SLG on (a) SiO_2/Si and (b) infinitely thick SiO_2. Ultrafast pump pulses (red) arrive from the top using a 0.7 NA objective in both configurations, while HotPL (green and blue in a and b, respectively) is collected in back-reflection through the same objective in (a) and in transmission through a 0.85 NA objective in (b). c, d) HotPL spectra (thin lines) and fits (thick lines) from CVD-SLG for the configurations sketched in (a,b), respectively. The fits are obtained from Eq.1 by adjusting T_e, ξ and δ. ξ is (c) ~ 100 and (d) ~ 4000. δ varies between -5 and -16 cts/s depending on the impinging fluence. e) $S(\lambda)$ is calculated for the various substrates using a dipole located 2 nm above SiO_2/Si (light green, middle inset), SiO_2 (blue, top inset) and inside a double layer of hBN (orange, bottom inset). Inset: pump power ratio impinging on the SLG as a function of wavelength for SiO_2 (blue) and SiO_2/Si (green), calculated by dividing the effective power deposited on SLG due to the presence of the substrate with that exiting the objective.

2 to collect light in transmission. To efficiently collect the nonlinear emission, which is mostly directed towards the glass substrate, we insert a 0.85 NA air objective at the opposite side of the sample with respect to the illumination objective, as illustrated in Fig. 5b. The collected light is then redirected to the same detection path. The background-subtracted HotPL spectra from CVD-SLG on SiO_2/Si and SiO_2, as a function of pump fluence, are in Figs. 5c (green) and 5d (blue), respectively.

To model the data, we first numerically estimate how the photonic environment reshapes the HotPL spectrum emitted by SLG. This is done by considering the emission from an electric dipole placed 2 nm above the substrate (either a semi-infinite glass plane or a thin SiO_2/Si film). The dipole is oriented parallel to the substrate surface and its emission within the NA of the collection objective is evaluated with FDTD. This gives a set of spectral response functions, $S(\lambda)$, for the different substrates (Fig. 4e). For a semi-infinite SiO_2 substrate the spectral response is almost flat in the investigated wavelength range (blue line), while the emission is significantly reshaped for SiO_2/Si (light green line), which acts as a broadband photonic cavity.

We apply a similar approach to evaluate the reshaping effect for hBN/SLG/hBN. In this case the simulated emitting dipole is inserted in the center of a 20nm hBN slab with refractive index n = 2.17 [72,73]. hBN shifts the position of the dipole with respect to the SiO_2/Si photonic cavity, resulting in a red shift of the emission peak (orange line in Fig. 5e).

Semiclassical PL theories yield the profile of the emitted light, but not the overall intensity [19], as the latter depends on the interaction between e and quantized modes of the electromagnetic spectrum. Fully quantum theories [74] require the integration of quantum-mechanical equations of motion with sub-femtosecond accuracy. This is a substantial computational effort, given that HotPL is emitted for several hundreds of fs after pulsed excitation [19,20]. Following the pump pulse, the instantaneous intensity of the HotPL decreases in time, due to electron-hole (e-h) recombination and the cooling of the HE distribution. However, the time-integrated spectrum is dominated by the signal produced by the thermalized e distribution at its hottest temperature, i.e. at the end of the pump pulse

Although a full quantum treatment of the out-of-equilibrium system would be required, here we approximate it by the signal emitted by HEs immediately after photoexcitation. We express the collected HotPL intensity as the product of $S(\lambda)$ and a factor proportional to the SLG joint density of states (JDOS) at the emitted photon wavelength for a thermalized e-h distribution at T_e [24]:

$$I(\lambda, T_e) = S(\lambda) \cdot \xi \frac{2hc^2}{\lambda^5} \frac{1}{\left[e^{\left(\frac{hc}{2\lambda k_\mathrm{B} T_e}\right)} + 1 \right]^2} + \delta \tag{1}$$

In Eq.1, $\xi\frac{2hc^2}{\lambda^5}\frac{1}{\left[e^{\left(\frac{hc}{2\lambda k_\mathrm{B}T_e}\right)}+1\right]^2}$ is the JDOS multiplied by the Boltzmann distribution [24], through the dimensionless coefficient ξ. This depends on the oscillator strength of the direct transitions in the Dirac cones [24], parametrizing the overall intensity of the HotPL spectrum, integrated in time between pulses. Eq.1 is a reliable model for the HotPL in SLG as long as T_e is the same for both *e* and *h* and the photoexcited carrier density is much larger than the SLG doping [16,75], as in our case. In Eq.1, h is the Planck constant, *c* the speed of light in vacuum, k_B the Boltzmann constant, and λ the wavelength. δ [cts/s] is a constant introduced to correct for residual offsets after background subtraction. For short wavelengths ($\lambda \ll \frac{hc}{2k_\mathrm{B}T_e}$), the dominating term in Eq.1 is an exponential tail, similar to that obtained, in such a spectral range, from black body emission [19]. The fits using Eq.1 are superimposed to the data in Fig. 4c (solid green lines) and Fig. 4d (solid blue lines) for CVD-SLG on Si/SiO$_2$ and SiO$_2$, respectively. T_e is treated as an independent parameter. A univocal set of values for ξ and δ is used for each sample to attain the best fit. These values are allowed to vary for the different samples, since they depend on several experimental conditions (*e.g.* sample mounting, small deviations in optical setup alignment and background level). Our model allows to account for the variation of HotPL intensity with pump intensity through T_e, without need for further normalization. The HotPL intensity is a non-linear function of the pump intensity through T_e in our out-of-equilibrium model, while ξ is a constant proportionality factor that accounts for the experimental conditions, such as setup collection efficiency.

In both CVD-SLG samples T_e increases with pump fluence. Although the pump fluences for CVD-SLG on SiO$_2$/Si are lower than for CVD-SLG on SiO$_2$, the corresponding T_e is higher in the first case. This can be ascribed to the influence of the photonic cavity created by SiO$_2$/Si on the 1554-nm pump beam which, as confirmed by FDTD (inset of Fig. 5e), enhances the pump fluence by a factor ~ 2. The agreement between model and experiments for both data sets validates our approach.

2.3. Tuning the HotPL emission by out-of-plane heat transfer

To demonstrate the possibility of engineering the HotPL via out-of-plane heat transfer, we investigate with our model the HotPL emission of three different samples: MC-SLG, CVD-SLG and hBN/SLG/hBN. Figs. 6a-c plot the HotPL spectra as a function of the incident fluence, accounting for the enhancement induced by the substrate (see inset in Fig. 5e). For each sample, all spectra are fitted using Eq.1 and optimizing T_e, ξ and δ. While ξ is not sensitive to fluence, δ changes with it. This could be ascribed to an imperfect background compensation. The excellent agreement between model and experiments demonstrates the robustness of this approach, once the photonic environment and the substrate are accounted for. The fluence-dependent T_e plots in Fig. 6d show that MC- and CVD-SLG reach a similar $T_e \sim$ 2200-2300 K for a pump fluence ~4.9 J/m^2, consistent with T_e of Refs. [16, 19]. Despite small deviations, which we ascribe to different E_F, the observation of similar T_e for the same illuminating fluence implies that the fabrication process and doping do not significantly affect the electron dynamics and the nonlinear optical response in our experimental conditions. The experimental data are integrated over the whole emission decay time [19], while the calculations consider only the emission in the instant of time when T_e is the highest.

For hBN/SLG/hBN a significant drop in T_e is observed (see Fig. 6d), as reflected in the red-shift of the emission spectrum (see Fig. 6c), which can only be partially attributed to the photonic response of hBN/SLG/hBN (orange curve in Fig.5e), which is different from that on bare SiO_2/Si (green curve in Fig. 5e). The almost 2-fold reduction in T_e calls for further underlying physical processes associated with SLG encapsulation in hBN. In hBN/SLG/hBN, out-of-plane heat transfer can occur between SLG and hBN thanks to near-field coupling between SLG HEs and the hyperbolic phonons in hBN [76,77]. This offers an efficient cooling channel, associated with a significant reduction of the SLG HE lifetime [35,76,77].

Therefore, the overall red shift in the SLG HotPL caused by the encapsulation with hBN can be interpreted as due to the combination of two effects: (i) a purely photonic one, associated with the presence of the two high refractive index hBN layers that produce an emission spectral reshaping; (ii)

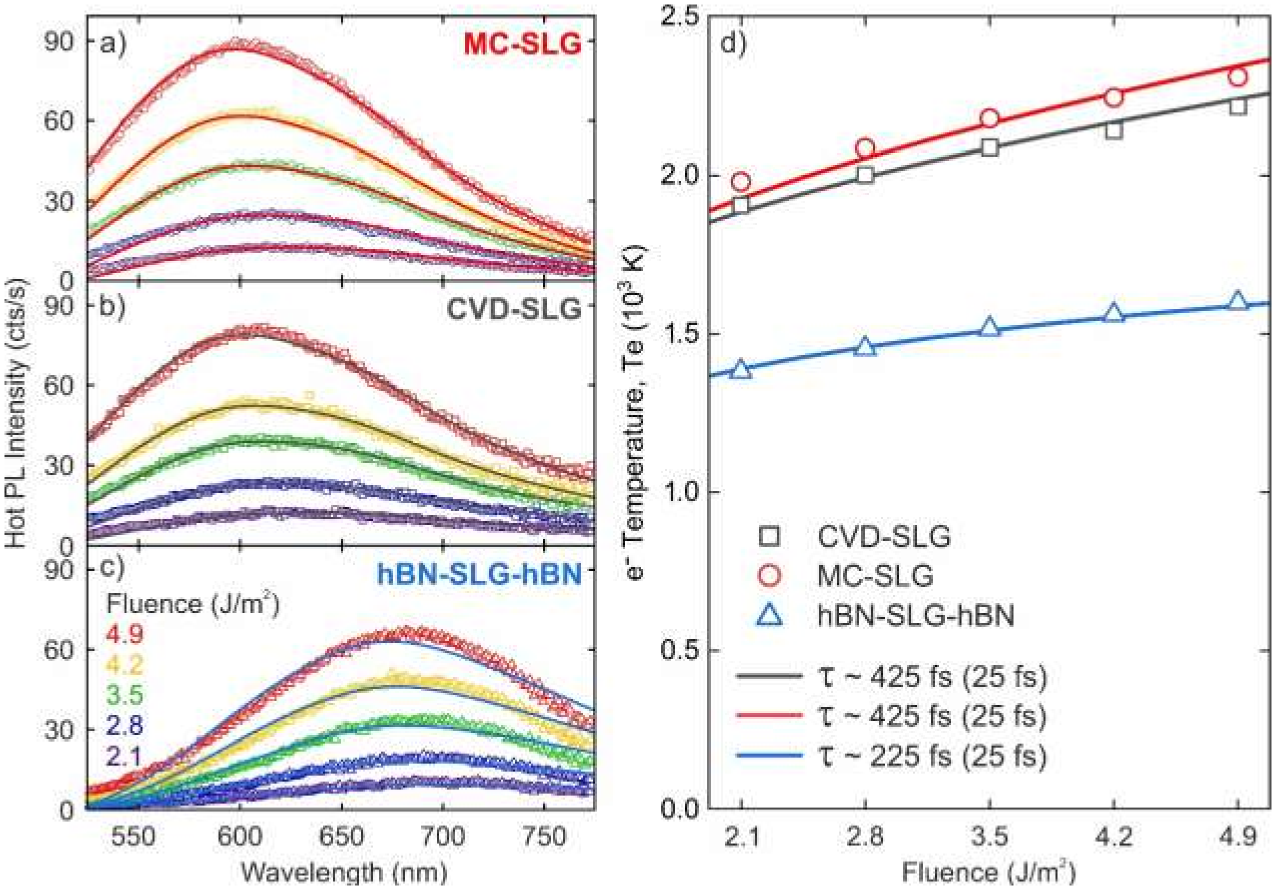

Figure 6. (a-c) Fluence-dependent HotPL for (a) MC-SLG, (b) CVD-SLG and (c) hBN/SLG/hBN and fits from Eq.1. The spectra in (a-c) are collected using pump fluencies ~ 2.1 (violet), 2.8 (blue), 3.5 (green), 4.2 (yellow), 4.9 J/m^2 (red), the same as in (d). d) Fluence-dependence of T_e extracted from the fits. (a-c) also show the fits for MC-SLG (solid red line), CVD-SLG (solid grey line) and hBN/SLG/hBN (solid light blue line), obtained varying δ from -7 to -34 cts/s. ξ provides the best fits for values of 25 (MC-SLG and CVD-SLG) and 800 (hBN/SLG/hBN). The solid lines represent T_e from the model in Refs. 16, 17. τ is searched on a mesh with a step of 25 fs, which sets the fit uncertainty.

a more fundamental one, consisting in the modification of the thermal properties of HEs in SLG by the presence of the heat-sink consisting in the near-field coupling to hyperbolic phonons in hBN. Although a lower T_e can be related to the observed HotPL red-shift (Figs. 5a-c), the quantitative evaluation of T_e can be done only if the photonic response of the whole heterostructure is considered.

To further support these observations, we estimate the expected T_e using the model of Refs. 78,79 based on a set of rate equations for T_e and the photoexcited carrier density in SLG, solved in the steady-state regime. Dissipation is accounted for in the relaxation-time approximation, parametrized by a cooling time τ. The absorption coefficient α [80] includes a saturable, T_e-dependent contribution, due to inter-band vertical transitions [6], and a residual, non-saturable, constant contribution α_{res} [81]. α_{res} corresponds to a "residual" absorbance in the Pauli-blocked regime [81]. In the case of non-encapsulated SLG, this is of the same order of magnitude as the non-saturable absorption $\alpha_{\mathrm{NS}}\sim$ 0.8% [6]. We apply this model to fit the T_e dependence on the illumination fluence, finding $\tau\sim$ 425 fs for CVD- and MC-SLG, and $\tau\sim$ 225 fs for hBN/SLG/hBN. The uncertainty in the determination of τ is dictated by the mesh step of 25 fs in our model.

This shorter relaxation time can be ascribed to the coupling with the hBN hyperbolic phonons. We also find $\alpha_{\mathrm{res}}\sim$ 0.08% for hBN/SLG/hBN, and a larger $\alpha_{\mathrm{res}}\sim$ 0.4 %, 0.5 % for CVD and MC-SLG, respectively. We use in the model a single T_e for both HEs and hot h, since we assume the time-integrated spectra to be dominated by the signal produced by the thermalized e distribution at its highest T_e, i.e. at the end of pump pulse. Therefore, the model describes the steady state of the carriers under the action of heating, due to the pump pulse, and cooling, due to coupling with phonons.

2.4. THG dependence on the electron temperature in SLG

Finally, we explore the impact of the different E_{F} and T_e on THG emission, by comparing the THG fluence dependence in the three samples. After subtracting the HotPL contribution from the nonlinear emission spectra, we obtain the THG spectra in Figs.7a-c. The fluence-dependent wavelength-integrated THG powers, plotted in log-log scale in Fig. 7d, reveals a slope that exceeds the expected 3 [70], in agreement with Ref. 17, where we reported a sizable deviation from the typical cubic power law for THG caused by the dependence of the nonlinear susceptibility on both T_e and E_{F}. In our experiments, E_{F} ~0.3 eV for CVD-SLG, ~0.18 eV for MC-SLG and ~0.09 eV for hBN/SLG/hBN (see Table 1), hence E_{F} is much smaller than the pump photon energy (~ 0.8 eV). This condition makes the THG process extremely sensitive to T_e. As we discussed in Ref. 17, for $E_{\mathrm{F}} < h\nu/2$, η^{THG} is expected to grow with T_e, therefore resulting in a power law with an exponent larger

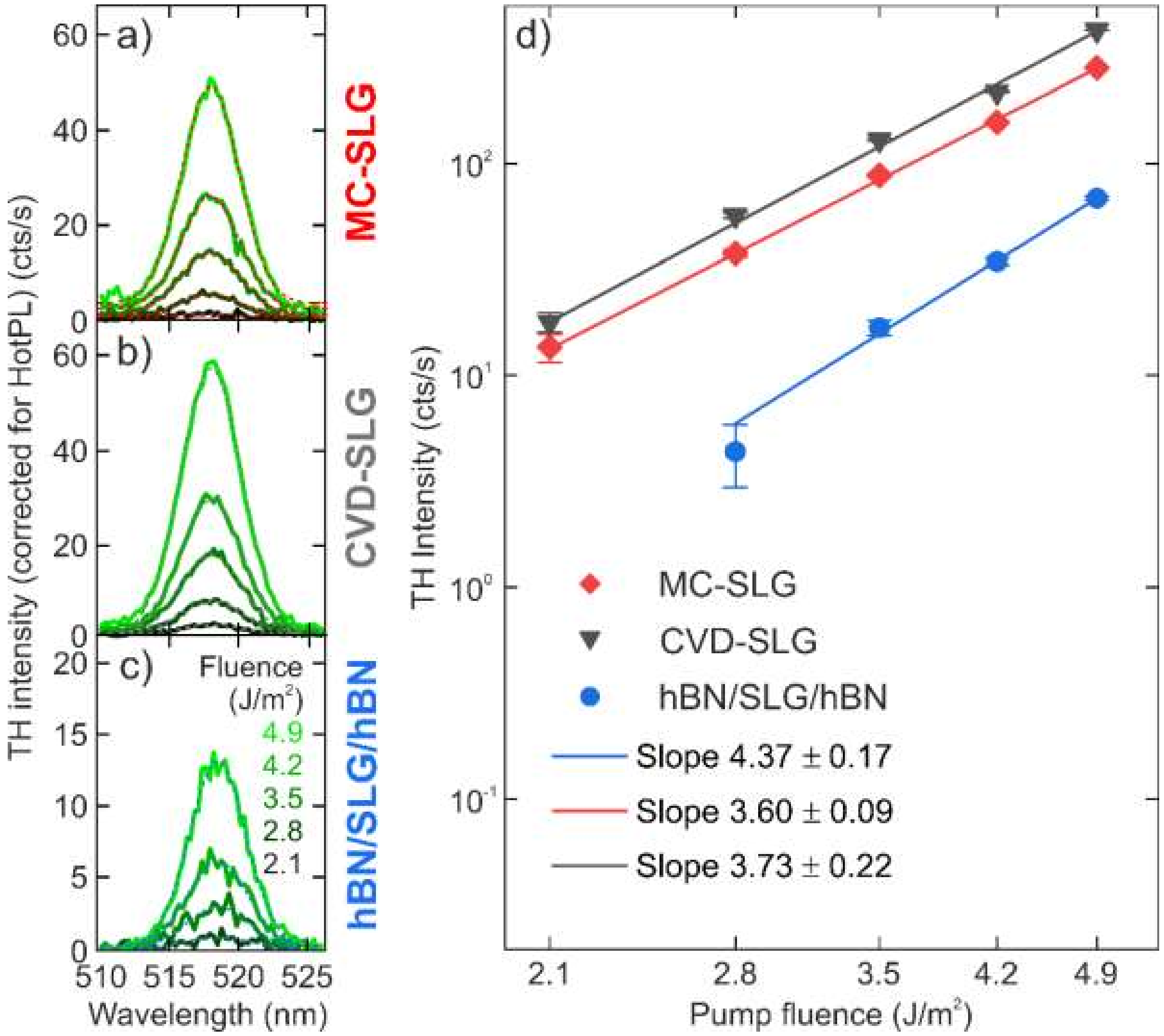

Figure 7. Fluence dependence of TH generation. Fluence dependent TH spectra of (a) MC-SLG, (b) CVD-SLG and (c) hBN/SLG/hBN after subtraction of HotPL background. The red, grey and blue dashed lines are Gaussian fits. (d) TH powers, measured as the areas under the Gaussian curves in panels (a-c), as a function of pump fluence. Solid lines are fits with power law curves.

than 3. The lower T_e in hBN/SLG/hBN is accompanied by a higher THG power slope, compared to the other samples, in good agreement with our model in Ref. 16. In particular, as we discussed in the Supplementary Information of Ref. 16, the strongest variation of η^{THG} upon increasing photoexcitation fluence is expected for $T_{\mathrm{e}} < 1800$ K and $E_{\mathrm{F}}/h\nu << 1$, which exactly overlap the working conditions identified for the hBN/SLG/hBN sample. The THG signal from hBN/SLG/hBN is reduced by a factor~2, when compared to that of MC-SLG and CVD-SLG, due to cavity effects (see Fig.5e). However, this does not affect the slope in Fig.7, hence the evaluation of the effects of T_e on η^{THG}.

3. Conclusions

We measured the broadband light emission of different graphene samples following ultrashort pulse excitation. We modelled the spectra by combining the emission from an out-of-equilibrium hot electron bath and the photonic environment of graphene, also taking the response of the collection optics into account. We found that both the substrate (via photonic cavity effects) and the increase of the electronic temperature contribute to a stark shaping of the HotPL emission, as well as of the THG efficiency. We derived the dependence of the electronic temperature on the incident fluence. Under similar illumination conditions, hBN-encapsulated graphene (hBN/SLG/hBN) shows a substantially lower electronic temperature than the other samples, due to the coupling of SLG hot electrons with hBN hyperbolic phonons. The hot electron temperature influences also the dependence of the emitted third harmonic intensity on pump fluence, giving a power law with exponent >3 [17]. Thus, in SLG, both incoherent (HotPL) and coherent (THG) emission are extremely sensitive to the electronic temperature. This must be considered in ultrafast all-optical applications of SLG-based devices, such as tunable broadband light emitters and nonlinear frequency converters. Our results clarify the interplay between hot electrons and optical nonlinear effects in graphene and can be used to tailor the emission wavelength and temperature of graphene-based high-speed broadband light emitters. Our approach can be extended to reproduce the incoherent emission from any layered material coupled to any substrate.

Acknowledgements

We acknowledge funding from EU Graphene and Quantum Flagships, ERC Grants Hetero2D, GSYNCOR, EPSRC Grants EP/N010345/1, EP/L016087/1, the Elemental Strategy Initiative conducted by the MEXT, Japan, Grant Number JPMXP0112101001, JSPS KAKENHI Grant Number JP20H00354 and the CREST(JPMJCR15F3), JST.

References

1. Ferrari A C et al. 2015 Science and technology roadmap for graphene, related two-dimensional crystals, and hybrid systems *Nanoscale* **7** 4598-4810
2. Bonaccorso F, Sun Z, Hasan T, and Ferrari A C 2010 Graphene photonics and optoelectronics *Nat. Photonics* **4** 611-622
3. Romagnoli M, Sorianello V, Midrio M, Koppens F H L, Huyghebaert C, Neumaier D, Galli P, Templ W, D'Errico A and Ferrari A C 2018 Graphene-based integrated photonics for next-generation datacom and telecom *Nat. Rev. Mater.* **3** 392-414.
4. Liu M, Yin X, Ulin-Avila E, Geng B, Zentgraf T, Ju L, Wang F, and Zhang X 2011 A graphene-based broadband optical modulator *Nature* **474** 64-67
5. Sorianello V, Midrio M, Contestabile G, Asselberghs I, Van Campenhout J, Huyghebaert C, Goykhman I, Ott A K, Ferrari A C, and Romagnoli M 2018 Graphene-silicon phase modulators with gigahertz bandwidth *Nat. Photonics* **12** 40-44
6. Sun Z, Hasan T, Torrisi F, Popa D, Privitera G, Wang F, Bonaccorso F, Basko D M, and Ferrari A C 2010 Graphene Mode-Locked Ultrafast Laser *ACS Nano* **4** 803-810
7. Grigorenko A N, Polini M, Novoselov K S 2012 Graphene plasmonics *Nat. Photonics* **6** 749–758
8. Koppens F H L, Chang D E, García de Abajo F J 2011 Graphene Plasmonics: A Platform for Strong Light–Matter Interactions *Nano Lett*. **118** 3370-3377
9. Koppens F H L, Mueller T, Avouris P, Ferrari A C F, Vitiello M S, Polini M 2014 Photodetectors based on graphene, other two-dimensional materials and hybrid systems *Nat. Nanotechnol.* **9** 780-793
10. Vicarelli L, Vitiello M S, Coquillat D, Lombardo A, Ferrari A C, Knap W, Polini M, Pellegrini V, and Tredicucci A 2012 Graphene field-effect transistors as room-temperature terahertz detectors *Nat. Mater.* **11** 865-871

11. Mueller T, Xia F, and Avouris P 2010 Graphene photodetectors for high-speed optical communications *Nat. Photonics* **4** 297-301

12. Goykhman I, Sassi U, Desiatov B, Mazurski N, Milana S, de Fazio D, Eiden A, Khurgin J, Shappir J, Levy U, and Ferrari A C 2016 On-Chip Integrated, Silicon–Graphene Plasmonic Schottky Photodetector with High Responsivity and Avalanche Photogain *Nano Lett.* **16** 3005-3013

13. De Fazio D, Goykhman I, Yoon D, Bruna M, Eiden A, Milana S, Sassi U, Barbone M, Dumcenco D, Marinov K, Kis A, and Ferrari A C 2016 High Responsivity, Large-Area Graphene/MoS_2 Flexible Photodetectors *ACS Nano* **10** 8252-8262

14. Nair R R, Blake P, Grigorenko A N, Novoselov K S, Booth T J, Stauber T, Peres N M R, Geim A K 2008 Fine structure constant defines visual transparency of graphene *Science* **320** 1308

15. Mak K F, Sfeir M Y, Wu Y, Lui C H, Misewich J A, Heinz T F 2008 Measurement of the Optical Conductivity of Graphene *Phys. Rev. Lett.* **101** 196405

16. Soavi G, Wang G, Rostami H, Purdie D G, De Fazio D, Ma T, Luo B, Wang J, Ott A K, Yoon D, Bourelle S A, Muench J E, Goykhman I, Dal Conte S, Celebrano M, Tomadin A, Polini M, Cerullo G, and Ferrari A C 2018 Broadband, electrically tunable third-harmonic generation in graphene *Nat. Nanotechnol.* **13** 583-588

17. Soavi G, Wang G, Rostami H, Tomadin A, Balci O, Paradisanos I, Pogna E A A, Cerullo G, Lidorikis E, Polini M, and Ferrari A C 2019 Hot Electrons Modulation of Third-Harmonic Generation in Graphene *ACS Photonics* **6** 2841–2849

18. Jiang T, Huang D, Cheng J, Fan X, Zhang Z, Shan Y, Yi Y, Dai Y, Shi L, Liu K, Zeng C, Zi J, Sipe J E, Shen Y-R, Liu W-T, and Wu S 2018 Gate-tunable third-order nonlinear optical response of massless Dirac fermions in graphene *Nat. Photonics* **12** 430-436

19. Lui C H, Mak K F, Shan, J and Heinz T F 2010 Ultrafast Photoluminescence from Graphene *Phys. Rev. Lett.* **105** 127404

20. Liu W-T, Wu S W, Schuck P J, Salmeron M, Shen Y R, and Wang F 2010 Nonlinear broadband photoluminescence of graphene induced by femtosecond laser irradiation *Phys. Rev. B* **82** 081408(R)
21. Freitag M, Chiu H-Y, Steiner M, Perebeinos V, and Avouris P 2010 Thermal infrared emission from biased graphene *Nat. Nanotechnol.* **5** 497-501
22. Chen C-F, Park C-H, Boudouris B W, Horng J, Geng B, Girit C, Zettl A, Crommie M F, Segalman R A, Louie S G, and Wang F 2011 Controlling inelastic light scattering quantum pathways in graphene *Nature* **471** 617-620
23. Li T, Luo L, Hupalo M, Zhang J, Tringides M C, Schmalian J, and Wang J 2012 Femtosecond Population Inversion and Stimulated Emission of Dense Dirac Fermions in Graphene *Phys. Rev. Lett.* **108**, 167401
24. Kim Y D et al. 2015 Bright visible light emission from graphene *Nat. Nanotechnol.* **10**, 676
25. Huang D, Jiang T, Zhang Y, Shan Y, Fan X, Zhang Z, Dai Y, Shi L, Liu K, Zeng C, Zi J, Liu W-T, and Wu S 2018 Gate Switching of Ultrafast Photoluminescence in Graphene *Nano Lett.* **18** 79-85
26. Kim Y D, Gao Y, Shiue R-J, Wang L, Aslan O B, Bae M-H, Kim H, Seo D, Choi H-J, Kim S H, Nemilentsau A, Low T, Tan C, Efetov D K, Taniguchi T, Watanabe K, Shepard K L, Heinz T F, Englund D, and Hone J 2018 Ultrafast Graphene Light Emitters *Nano Lett.* **18** 934-940
27. Shiue R-J, Gao Y, Tan C, Peng C, Zheng J, Efetov D K, Kim Y D, Hone J, and Englund D 2019 Thermal radiation control from hot graphene electrons coupled to a photonic crystal nanocavity *Nat. Commun.* **10** 109
28. Mak K F, Ju L, Wang F, Heinz T F 2012 Optical spectroscopy of graphene: From the far infrared to the ultraviolet *Solid State Commun.* **152** 1341-1349
29. Handloser M, Piredda G, Lombardo A, Ferrari A C, Hartschuh A 2011 Non-linear Photoluminescence from Graphene *OSA Technical Digest*, JSII1_2 (2011)

30. Castro Neto A H, Guinea F, Peres N M R, Novoselov K S, Geim A K 2009 The electronic properties of graphene *Rev. Mod. Phys.* **81** 109
31. Bahk Y-M, Ramakrishnan G, Choi J, Song H, Choi G, Kim Y H, Ahn K J, Kim D-S, and Planken P C M 2014 Plasmon Enhanced Terahertz Emission from Single Layer Graphene *ACS Nano* **8** 9089
32. Miyoshi Y, Fukazawa Y, Amasaka Y, Reckmann R, Yokoi T, Ishida K, Kawahara K, Ago H, and Maki H 2018 High-speed and on-chip graphene blackbody emitters for optical communications by remote heat transfer *Nat. Commun.* **9** 1279
33. Shi C, Mahlmeister N H, Luxmoore I J, and Nash G R 2018 Metamaterial-based graphene thermal emitter. *Nano Res.* **11**, 3567–3573
34. Stöhr R J, Kolesov R, Pflaum J, and Wrachtrup J 2010 Fluorescence of laser-created electron-hole plasma in graphene *Phys. Rev. B* **82** 121408(R)
35. Brida D, Tomadin A, Manzoni C, Kim Y J, Lombardo A, Milana S, Nair R R, Novoselov K S, Ferrari A C, Cerullo G and Polini M 2013 Ultrafast collinear scattering and carrier multiplication in graphene *Nat. Commun.* **4** 1987
36. Breusing M, Kuehn S, Winzer T, Malić E, Milde F, Severin N, Rabe J P, Ropers C, Knorr A, and Elsaesser T 2011 Ultrafast nonequilibrium carrier dynamics in a single graphene layer *Phys. Rev. B* **83** 153410
37. Lazzeri M, Piscanec S, Mauri F, Ferrari A C, and Robertson J 2005 Electron Transport and Hot Phonons in Carbon Nanotubes *Phys. Rev. Lett.* **95** 236802
38. Sun D, Wu Z-K, Divin C, Li X, Berger C, de Heer W A, First P N, and Norris T B 2008 Ultrafast Relaxation of Excited Dirac Fermions in Epitaxial Graphene Using Optical Differential Transmission Spectroscopy *Phys. Rev. Lett.* **101**, 157402
39. Lawton L M, Mahlmeister N H, Luxmoore I J, and Nash G R 2014 Prospective for graphene based thermal mid-infrared light emitting devices *AIP Advances* **4**, 087139

40. Lochbaum A., Fedoryshyn Y, Dorodnyy A, Koch U, Hafner A, and Leuthold J On-Chip Narrowband Thermal Emitter for Mid-IR Optical Gas Sensing 2017 *ACS Photon.* **4**, 1371–1380

41. Safei A, Chandra S, Leuenberger M N, and Chanda D 2019 Wide Angle Dynamically Tunable Enhanced Infrared Absorption on Large-Area Nanopatterned Graphene *ACS Nano* **13,** 421-428

42. Gu T, Petrone N, McMillan J F, van der Zande A, Yu M, Lo G Q, Kwong D L, Hone J., and Wong C W 2012 Regenerative oscillation and four-wave mixing in graphene optoelectronics *Nat. Photon.* **6**, 554-559.

43. Inoue T, De Zoysa M, Asano T, and Noda S 2015 Realization of narrowband thermal emission with optical nanostructures *Optica* **2**, 27

44. Inoue T, De Zoysa M, Asano T, and Noda S 2013 Single-peak narrow-bandwidth mid-infrared thermal emitters based on quantum wells and photonic crystals *Appl. Phys. Lett.* **102**, 191110

45. Thongrattanasiri S, Koppens F H L, and García de Abajo J 2012 Complete Optical Absorption in Periodically Patterned Graphene Phys. Rev. Lett. **108**, 047401

46. Fan Y, Liu Z, Zhang F, Zhao Q, Wei Z, Fu Q, Li J, Gu C, and Li H 2015 Tunable mid-infrared coherent perfect absorption in a graphene meta-surface *Sci. Rep.* **5** 13956

47. Novoselov K S, Jiang D, Schedin F, Booth T J, Khotkevich V V, Morozov S V, and Geim A K 2005 Two-dimensional atomic crystals *Proc. Natl. Acad. Sci. U.S.A.* **102** 10451

48. Li X, Cai W, An J, Kim S, Nah J, Yang D, Piner R, Velamakanni A, Jung I, Tutuc E, Banerjee S K, Colombo L and Ruoff R S 2009 Large-Area Synthesis of High-Quality and Uniform Graphene Films on Copper Foils *Science* **324**, 1312-1314

49. Bonaccorso F, Lombardo A, Hasan T, Sun Z, Colombo L, Ferrari A C 2012 Production and processing of graphene and 2d crystals *Mater. Today* **15** 564

50. Backes C et al. 2020 Production and processing of graphene and related materials *2D Mater. 7*, 022001

51. Taniguchi T and Watanabe K 2007 Synthesis of High-Purity Boron Nitride Single Crystals under High Pressure by using Ba–BN Solvent *J. Cryst. Growth* **303** 525-529
52. Casiraghi C, Hartschuh A, Lidorikis E, Qian H, Harutyunyan H, Gokus T, Novoselov K S and Ferrari A C 2007 Rayleigh Imaging of Graphene and Graphene Layers *Nano Lett.* **7** 2711-2717
53. Reich S, Ferrari A C, Arenal R, Loiseau A, Bello I, Robertson J 2005 Resonant Raman scattering in cubic and hexagonal boron nitride *Phys. Rev. B* **71** 205201
54. Ferrari A C, Meyer J C, Scardaci V, Casiraghi C, Lazzeri M, Mauri F, Piscanec S, Jiang D, Novoselov K S, Roth S, and Geim A K 2006 Raman Spectrum of Graphene and Graphene Layers *Phys. Rev. Lett.* **97** 187401
55. Arenal R, Ferrari A C, Reich S, Wirtz L, Mevellec J-Y, Lefrant S, Rubio A, and Loiseau A 2006 Raman spectroscopy of single-wall boron nitride nanotubes *Nano. Lett.* **6** 1812–1816
56. Purdie D G, Pugno N M, Taniguchi T, Watanabe K, Ferrari A C and Lombardo A 2018 Cleaning interfaces in layered materials heterostructures *Nat. Commun.* **9** 5387
57. Hong X, Zou K, and Zhu J 2009 Quantum scattering time and its implications on scattering sources in graphene *Phys. Rev. B* **80** 241415
58. Burson K M, Cullen W G, Adam S, Dean C R, Watanabe K, Taniguchi T, Kim P, and Fuhrer M S 2013 Direct imaging of charged impurity density in common graphene substrates *Nano Lett.* **13** 3576-3580
59. Lagatsky A A, Sun Z, Kulmala T S, Sundaram R S, Milana S, Torrisi F, Antipov O L, Lee Y, Ahn J H, Brown A C T, Sibbett W, and Ferrari A C 2013 2 μm solid-state laser mode-locked by single-layer graphene *Appl. Phys. Lett.* **102** 013113
60. Das A, Pisana S, Chakraborty B, Piscanec S, Saha S K, Waghmare U V, Novoselov K S, Krishnamurthy H R, Geim A K, Ferrari A C, and Sood A K 2008 Monitoring dopants by Raman scattering in an electrochemically top-gated graphene transistor *Nat. Nanotechnol.* **3** 210-215

61. Basko D M, Piscanec S, and Ferrari A C 2009 Electron-electron interactions and doping dependence of the two-phonon Raman intensity in graphene *Phys. Rev. B* **80** 165413
62. Mohiuddin T M G, Lombardo A, Nair R R, Bonetti A, Savini G, Jalil R, Bonini N, Basko D M, Galiotis C, Marzari N, Novoselov K S, Geim A K, Ferrari A C 2009 Uniaxial strain in graphene by Raman spectroscopy: G peak splitting, Grüneisen parameters, and sample orientation *Phys. Rev. B* **79**, 205433
63. Yoon D, Son Y-W, Cheong H 2011 Strain-Dependent Splitting of the Double-Resonance Raman Scattering Band in Graphene. *Phys. Rev. Lett.* **106**, 155502 (2011).
64. Pisana S, Lazzeri M, Casiraghi C, Novolesov K S, Geim A K, Ferrari A C 2007 Breakdown of the adiabatic Born–Oppenheimer approximation in graphene. *Nature Mater* **6**, 198–201
65. Bruna M, Ott A K, Ijäs M, Yoon D, Sassi U, Ferrari A C 2014 Doping Dependence of the Raman Spectrum of Defected Graphene *ACS Nano* **8**, 7432-7441
66. Cançado L G, Jorio A, Martins Ferreira E H, Stavale F, Achete C A, Capaz R B, Moutinho M V O, Lombardo A, Kulmala T S and Ferrari A C 2011 Quantifying Defects in Graphene via Raman Spectroscopy at Different Excitation Energies *Nano Lett*. **11** 3190-3196
67. Sullivan D M 2013 Electromagnetic Simulation Using the FDTD Method 2nd edition (John Wiley and Sons, Inc., Hoboken, New Jersey)
68. Bozhevolnyi S I, Beermann J and Coello V 2003 Direct Observation of Localized Second-Harmonic Enhancement in Random Metal Nanostructures *Phys. Rev. Lett.* **90** 197403
69. Baraban A P, Samarin S N, Prokofiev V A, Dmitriev V A, Selivanov A A, Petrov Y 2019 Luminescence of SiO_2 layers on silicon at various types of excitation *J. Lumin.* **205** 102-108
70. Boyd R 2008 Nonlinear Optics 3rd edition Academic Press, Cambridge, Massachusetts
71. Roddaro S, Pingue P, Piazza V, Pellegrini V, Beltram F 2007 The Optical Visibility of Graphene: Interference Colors of Ultrathin Graphite on SiO_2 *Nano Lett*. **79**, 2707-2710

72. Schubert M, Rheinlander B, Franke E, Neumann H, Hann J, Order M, Richter F 1997 Anisotropy of boron nitride thin-film reflectivity spectra by generalized ellipsometry *Appl. Phys. Lett.* **70** 1819
73. Rah Y, Jin Y, Kim S and Yu K 2019 Optical analysis of the refractive index and birefringence of hexagonal boron nitride from the visible to near-infrared *Opt. Lett.* **44** 3797-3800
74. Kira M and Koch S W 2012 Semiconductor Quantum Optics (Cambridge University Press, Cambridge)
75. Tomadin A, Hornett S M, Wang H I, Alexeev E M, Candini A, Coletti C, Turchinovich D, Kläui M, Bonn M, Koppens F H L, Hendry E, Polini M, Tielrooij K-J 2018 The ultrafast dynamics and conductivity of photoexcited graphene at different Fermi energies *Science Advances* **4**, eaar5313
76. Tielrooij K-J et al. 2018 Out-of-plane heat transfer in van der Waals stacks through electron–hyperbolic phonon coupling *Nat. Nanotechnol.* **13** 41-46
77. Baudin E, Voisin C and Placais B 2020 Hyperbolic Phonon Polariton Electroluminescence as an Electronic Cooling Pathway *Adv. Funct. Mater.* **30** 1904783
78. Rana F, George P A, Strait J H, Dawlaty J, Shivaraman S, Chandrashekhar M and Spencer M G 2009 Carrier recombination and generation rates for intravalley and intervalley phonon scattering in graphene *Phys. Rev. B* **79** 115447
79. Wang H, Strait J H, George P A, Shivaraman S, Shields V B, Chandrashekhar M, Hwang J, Rana F, Spencer M G, Ruiz-Vargas C S and Park J 2010 Ultrafast relaxation dynamics of hot optical phonons in graphene *Appl. Phys. Lett.* **96** 081917
80. Grosso G and Pastori Parravicini G 2013 Solid State Physics (Academic Press)
81. Marini A, Cox J D, García de Abajo F J 2017 Theory of graphene saturable absorption *Phys. Rev. B* **95**, 125408